Developing a new innovative methodology to integrate geophysical techniques into characterization of potential CO_2 storage sites: Lopín structure (southern Ebro Basin, Spain)

C. Ayala*, B. Benjumea, J. F. Mediato, J. García-Crespo, P. Clariana, R. Soto, F. Rubio, C. Rey-Moral, E. L. Pueyo, J. Martín-León, A. G. García, P. Fernández-Canteli and R. Martínez-Orio

C. N. IGME – CSIC, c/ Ríos Rosas 23, 28003 Madrid, Spain

Present addresses: CA, Geosciences Barcelona – CSIC, C/ Lluis Solé i Sabarís s/n, 08028 Barcelona, Spain

CA, 0000-0001-8457-8253; BB, 0000-0002-0673-3411; JFM, 0000-0002-4333-1163; JG-C, 0000-0002-1149-2827; PC, 0000-0002-4168-2744; RS, 0000-0002-1929-8850; FR, 0000-0001-7912-3254; CR-M, 0000-0001-5124-2200; ELP, 0000-0001-8480-381X; JM-L, 0000-0002-2342-4872; AGG, 0000-0002-3385-3232; PF-C, 0000-0001-6703-5636; RM-O, 0000-0003-1778-617X

*Correspondence: c.ayala@igme.es

Abstract: One of the main challenges facing geological storage is to identify cost-effective methodological workflows for characterizing and monitoring geological storage sites. In the framework of the ALGECO2 project, led by the IGME (Geological and Mining Institute, Spain), a preliminary study of the Lopín site in the NE of Spain indicated conditions were promising for geological storage of CO_2. However, the poor quality of the legacy seismic reflection data precluded thorough characterization. Within the H2020 PilotSTRATEGY project, one of the possible selected target reservoirs was the Lopín structure. In order to characterize its geometry and physical properties as required to properly evaluate its storage potential, IGME applied a new emerging methodology that integrates reinterpreted reflection seismic data with newly acquired and interpreted gravity, passive seismic and petrophysical data. This methodology was successfully applied along one seismic profile. In this paper, we present the results of this integration as the first step towards characterizing the site and evaluating its suitability for storage.

On the path to energy transition and decarbonization, the scientific community had long ago identified carbon capture and storage (CCS) as one of the main mitigation technologies to meet the climate goals, such as the Paris Agreement, set at the United Nations Framework Convention on Climate Change (UNFCCC) Conference of the Parties in 2015 (United Nations 2015; e.g. Metz *et al.* 2005; Boot-Handford *et al.* 2014; Leung *et al.* 2014; Alcalde *et al.* 2018; Rogelj *et al.* 2018 and references therein).

To support the climate goals of Spain, between 2009 and 2014, IGME developed the ALGECO2 programme to identify potential structures for CO_2 storage in the country (García-Lobón *et al.* 2010; Arenillas *et al.* 2014). In the Ebro–Pyrenees region, 19 potential structures were identified in the first ALGECO2 phase, including the Lopín structure discussed in this paper. Only a few of these potential stores have been subjected to further exploration (García-Lobón *et al.* 2010; Pueyo *et al.* 2010; Arenillas *et al.* 2014). From these potential storage structures, the Caspe (Mediato *et al.* 2017) and the Linking Zone structures (Izquierdo-Llavall *et al.* 2014, 2019) are worth highlighting. In both cases, the subsequent exploration of these storage sites confirmed their lack of suitability and, accordingly, they were ruled out. However, one structure that was identified as a potential CO_2 storage reservoir in the framework of this project was Lopín, in the southern Ebro Basin. A preliminary characterization showed positive conditions for CO_2 storage (García-Lobón *et al.* 2010; Mediato *et al.* 2014, 2015). The Lopín-1 borehole, located in the area, confirms that there are several stratigraphic units that could act as CO_2 reservoirs, but it is necessary to define a geological structure where the reservoir is at a depth greater than 1000 m (Bachu 2003), and to confirm the structure has an effective seal. In the Lopín-1 borehole, the Buntsandstein facies lies at appropriate depth, and the overlying evaporitic facies offer a suitable seal. However, the reservoir's lateral continuity to define a closed geological structure is still

From: Miocic, J. M., Heinemann, N., Edlmann, K., Alcalde, J. and Schultz, R. A. (eds) 2023. *Enabling Secure Subsurface Storage in Future Energy Systems*. Geological Society, London, Special Publications, **528**, 227–243.
First published online January 23, 2023, https://doi.org/10.1144/SP528-2022-70

unknown. The poor quality of the available reflection seismic data precluded confident characterization of the structure to confirm this location as geological storage site. Further exploration was ruled out at that time. First by the STRATEGY CCUS project (2019–22) and later within the PilotSTRATEGY project (2021–26), both funded by the EU within the H2020 framework; the Lopín structure was highlighted and finally proposed for further study. Given time and budget constraints, a methodology based on cost-effective geophysical techniques (gravimetry and passive seismic methods), use of legacy seismic and borehole information together with petrophysical data is proposed. This follows the approach taken by Stannard *et al.* (2019, 2021), although here, the techniques are applied to the investigation of a possible CO_2 storage site instead of the characterization of a mineral deposit. Several authors have already integrated passive seismic and legacy reflection data (Benjumea *et al.* 2016) or gravimetry and passive seismic data (Mitjanas *et al.* 2021; Sgattoni and Castellaro 2021). However, to our knowledge, this is one of the first demonstrations of the integration of these techniques together with legacy reflection seismic, petrophysical and geological data, reducing the uncertainty of the resulting geological model.

In this paper, to test this new methodology, we generated a geological cross-section from seismic reflection interpretation and borehole information that was subsequently refined by gravity modelling. This modelling is constrained by petrophysical information of the area and the estimated depth to different seismic impedance contrasts identified using the H/V method (horizontal-to-vertical spectral ratio of ambient noise) and borehole velocity information.

Geological setting

The study area is located in the Ebro Basin, close to its southern margin (Fig. 1). The Ebro Basin is located on the northeastern region of the Iberian Peninsula (Fig. 1). It has a triangular shape and constitutes the foreland basin of the Pyrenees, the Iberian Chain and the Catalan Coastal Ranges located to the north, south and east, respectively. Basin formation started during the Paleocene through flexural subsidence related to the growth of these three mountain ranges (e.g. Pardo *et al.* 2004).

The sedimentary infill of the Ebro Basin reaches a thickness greater than 5500 m in the central part of its northern (Pyrenean) margin and, in the southern (Iberian) margin, sedimentary thickness reaches up to 3000 m (e.g. Alonso-Zarza *et al.* 2002; Pardo *et al.* 2004). Deformation associated with thrusting and folding in the Cenozoic deposits of the Ebro Basin is only visible at surface at the basin margins. This deformation varies from thin-skinned in the Pyrenean margin to thick-skinned in the Iberian and Catalan margins. Subsurface data show the existence of several structures affecting the Paleozoic and Mesozoic rocks below the Cenozoic horizontal deposits outcropping in the Ebro Basin (e.g. Arlegui and Simón 2001; Butillé *et al.* 2012; Mediato *et al.* 2017; Izquierdo-Llavall *et al.* 2019). These structures show evidence of movement during the Paleogene Period in the southern margin of the Ebro Basin (Butillé *et al.* 2012). According to Klimowitz (1992), the tectonic activity may even have affected Lower Miocene rocks. These structures are orientated parallel to the Iberian and Catalan deformation fronts, oriented NW–SE and NE–SW, respectively.

Stratigraphy

The Ebro Basin is mostly characterized by Cenozoic deposits with horizontal bedding at surface. The presence of several wells has enabled study of the subsurface basin infill (Jurado 1990). The underlying basement comprises rocks from the Paleozoic Period, most of them deformed and metamorphosed during the Late Carboniferous Variscan orogeny (Ábalos *et al.* 2002). Above the Variscan basement, Triassic sediments show the typical Germanic facies: Buntsandstein red beds, Muschelkalk dolostones, limestones and evaporites and Keuper evaporites and shales. The Buntsandstein facies, which constitutes the target reservoir series, are characterized by very irregular detrital sedimentation linked to the tilting of blocks and the formation of graben and horst structures, which resulted from a contemporaneous extension period (Sopeña *et al.* 1988). This Triassic succession contains several layered evaporite sequences with platform carbonates and fine-grained detrital interbeds. In the SE Ebro Basin, these Triassic evaporite sequences are represented by: (i) a thin basal evaporite layer up to 50 m (Röt facies), which comprises the seal of the Lopín structure; (ii) a thick succession of Middle Triassic evaporites (M2, middle Muschelkalk facies) up to 325 m; and (iii) a succession, up to 400 m thick, of continental evaporites and fine clastics that are Late Triassic in age (Keuper facies) (Jurado 1990; Ortí *et al.* 2017). These Middle and Upper Triassic evaporites successions could be potential secondary seals.

The oldest Jurassic rocks of the Ebro Basin constitute 50 m of dolomites (Imón Fm.) overlain by a cyclic anhydrite unit bearing dolomitic interbeds (Lécera Fm.) with a total thickness of 200–450 m (Jurado 1990; Gómez *et al.* 2007). This sequence is in turn overlain by a succession up to 300 m thick, comprising several shallow platform carbonate sequences. This succession contains dolomites, limestones and limestones with interbedded marls, and is overlain by the continental carbonate and

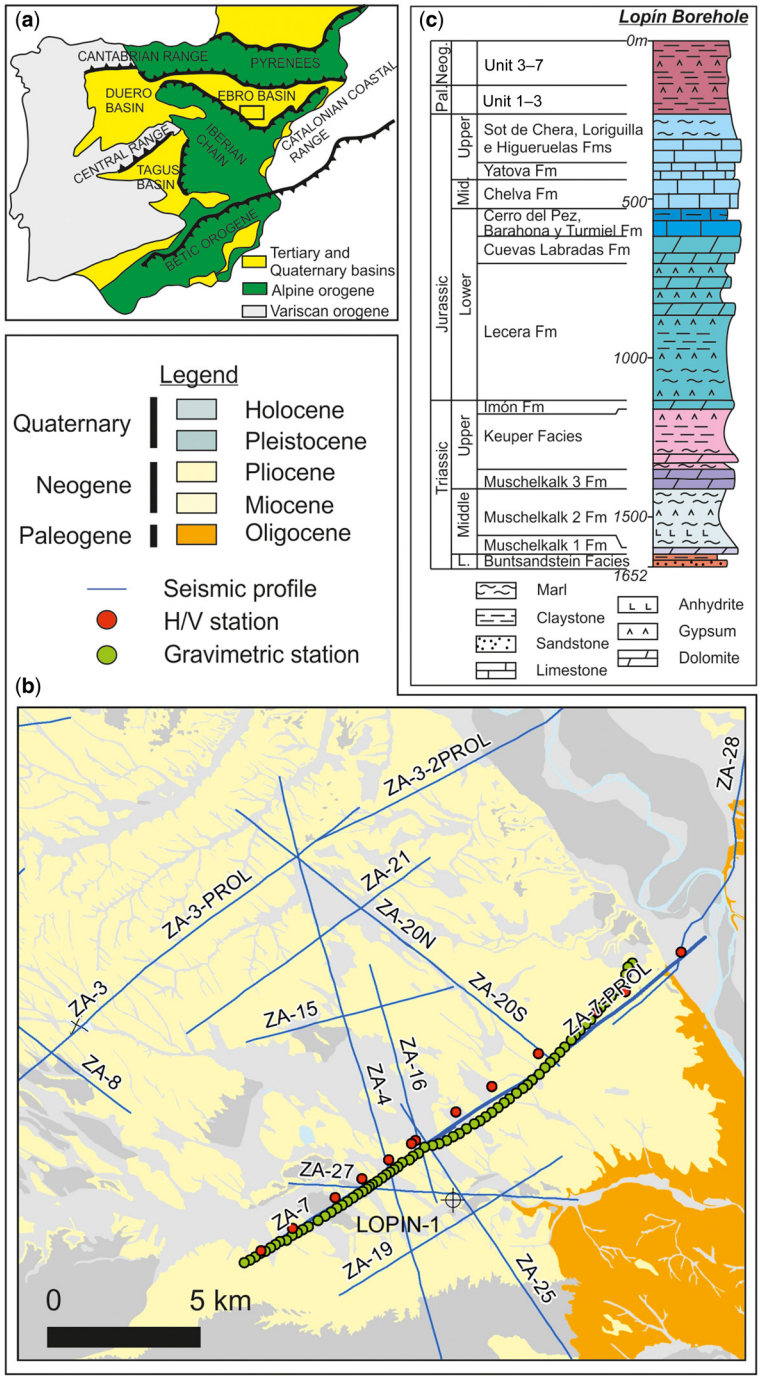

Fig. 1. (**a**) Map of the Iberian Peninsula with the main geological domains. (**b**) Geological map of the study area. Location of profiles ZA-7 and ZA-7-PROL is displayed: red points indicate H/V stations; green points correspond to gravity stations; blue line beneath the red and green points is the location of the seismic profile. Please note that H/V is the horizontal-to-vertical spectral ratio of ambient noise. (**c**) Stratigraphic column of Lopín-1 borehole.

detrital Cretaceous deposits. The Early Cretaceous strata are characterized by strong variations in the sedimentation linked to deformation during a rifting period (García-Quintana 1977). The base Cenozoic limit is unconformable and clearly observed in the seismic lines in the southern Ebro Basin. This erosional surface cuts into deposits of Cretaceous and Jurassic age. The Cenozoic succession is formed of continental evaporite and detrital sequences.

Data and methods

An innovative methodology was applied and consists of the integration of three geophysical techniques in the construction of an 18 km-long cross-section oriented SW–NE across the central part of the study area (see location in Fig. 1).

The workflow (Fig. 2) consisted of (1) building up a geological cross-section based on the interpretation of seismic reflection data and (2) gravity modelling of the cross-section with the additional applied constraints of the interpreted petrophysical and H/V data. This is an iterative feedback process that is complete when the model is consistent with all the observations: the outcome aligns with the gravity data, the corresponding horizons and the identified geological horizons on the seismic reflection profiles are located within the margins of uncertainty and within the limits of the H/V depths. Finally, the densities correspond to the calculated values from the petrophysical data and the final model is geologically valid and consistent with all available geological information for the area.

The aim of the current work is to validate the methodology of improving the interpretation through correlating the results from the three methods in order to obtain a unique geological model consistent with all available observations.

Seismic reflection data

The cross-section is anchored to a 2D depth-converted seismic reflection profile (see location in Fig. 1). The studied 2D seismic reflection profile corresponds to a composite line made of two individual profiles (lines ZA-7 and ZA-7-PROL, acquired in the 1970s and compiled from a public database repository, the Geophysical Information System of IGME-CSIC: info.igme.es/SIGEOF/). Both profiles were acquired with 48 channels and 10 Hz geophones. Receiver spacing was 80 and 40 m for ZA-07 and ZA-7-PROL, respectively. Sampling rate was 4 ms for both profiles. The seismic source used for ZA-07 acquisition was dynamite with a shot spacing of 120 m. ZA-07-PROL survey was designed with Vibroseis as a source with 40 m between shot points. The sweep length was 16 s and the sweep frequency was set up from 10 to 64 Hz.

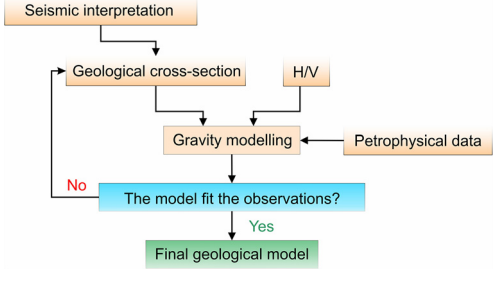

Fig. 2. Workflow of the methodology applied in this work.

The quality of the seismic section (Fig. 3) and its processing is low–medium, and it consists of a SEG-Y file vectorized from a TIFF file during the first ALGECO2 phase (García-Lobón *et al.* 2010). Interpretation of seismic horizons across the studied reflection seismic profile derives from a wider seismic survey (10E4-ZA regional, SSW–NNE- and NNW–SSE-oriented seismic lines that cover about 400 km in total length) and data from the Lopín-1 borehole located 2 km to the east of the studied seismic reflection profile (Fig. 1). Description of the lithology of the Lopín-1 well appears in Lanaja (1987), and density and sonic logs are also available at the SIGEOF database (info.igme.es/SIGEOF/). V_p and density logs are characterized by an alternating sequence of high and low velocity/density layers corresponding to the Middle to Late Jurassic and the first sector of the Early Jurassic down to 670 m (Fig. 4). This sequence overlies a more homogeneous layer characterized by high velocity and density values corresponding to the Lower Jurassic anhydrites. Velocity and density of Triassic strata depict high values for M1 and M3, and lower values for Keuper and M2 facies. This log information suggests that seismic techniques will allow us to image Lower Jurassic anhydrites as transparent zone and a sequence of reflections corresponding to Triassic sediments.

We performed time-to-depth conversion to avoid structural ambiguities and provide a depth basis for gravity modelling. Time-to-depth conversion was based on the average velocities used in the seismic processing for each line using SKUA-GOCAD19 (former Emerson, now Aspentech).

Several depth-based geological horizons were interpreted according to different reflectivity patterns and seismic facies. From Lopín-1 borehole top data and their correlation through the reflection seismic line, seven main seismic units are differentiated, from top to bottom (Fig. 3): (1) Cenozoic deposits, (2) Jurassic–Cretaceous deposits, (3) Hettangian limestones (Imón Fm), (4) Upper Triassic evaporites and lutites (Keuper facies), (5) Middle Triassic rocks

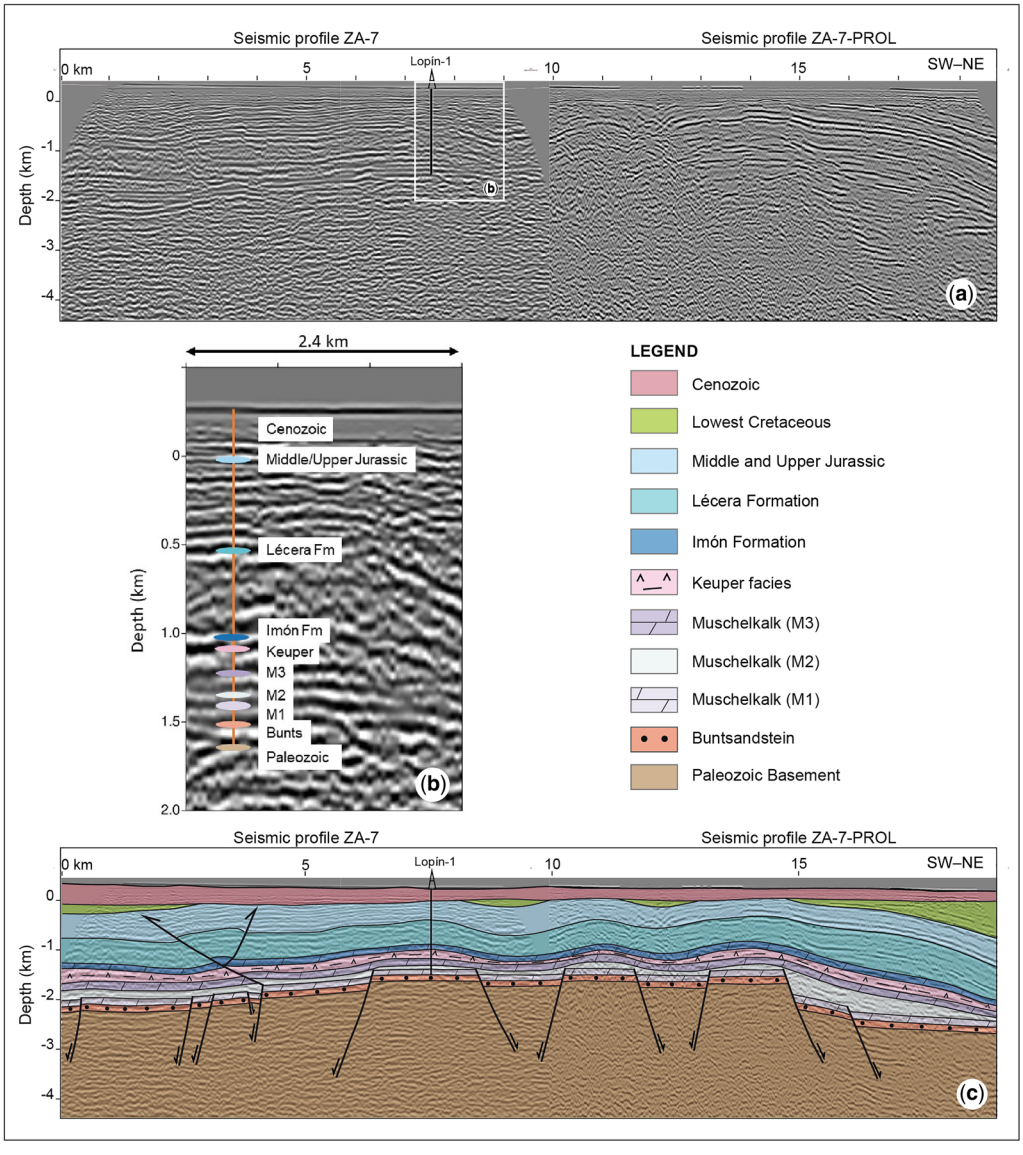

Fig. 3. (**a**) Depth-converted seismic profiles ZA-7 and ZA-7-PROL (no vertical exaggeration) showing the projection of Lopín-1 borehole. (**b**) Zoom in on the section of the profile where the projection of the Lopín-1 borehole is located and (**c**) initial geological interpretation.

(Muschelkalk facies) comprising M1, M2 and M3, (6) Lower Triassic rocks (Buntsandstein facies) and (7) Paleozoic basement rocks. The Paleozoic basement is characterized by a set of chaotic reflectors with scarce lateral continuity. The Buntsandstein facies are defined as a medium to highly disrupted reflector. The overlying unit represents the Muschelkalk facies and is divided into three sub-units: the M1 (dolostones) is characterized by a high-reflectivity package of two reflectors with relatively strong continuity; the M2 (Middle Triassic evaporites) are delineated by a poorly reflective to transparent package; and the M3 (dolostones) are represented, as the M1, by two reflectors with relatively high continuity. The overlying Upper Triassic evaporites (Keuper facies) are depicted by a poorly reflective package and, above these strata, a characteristic two high to medium reflectors define the Imón Formation dolostones. The marls, gypsums and anhydrites of the Lower Jurassic are characterized as a thick

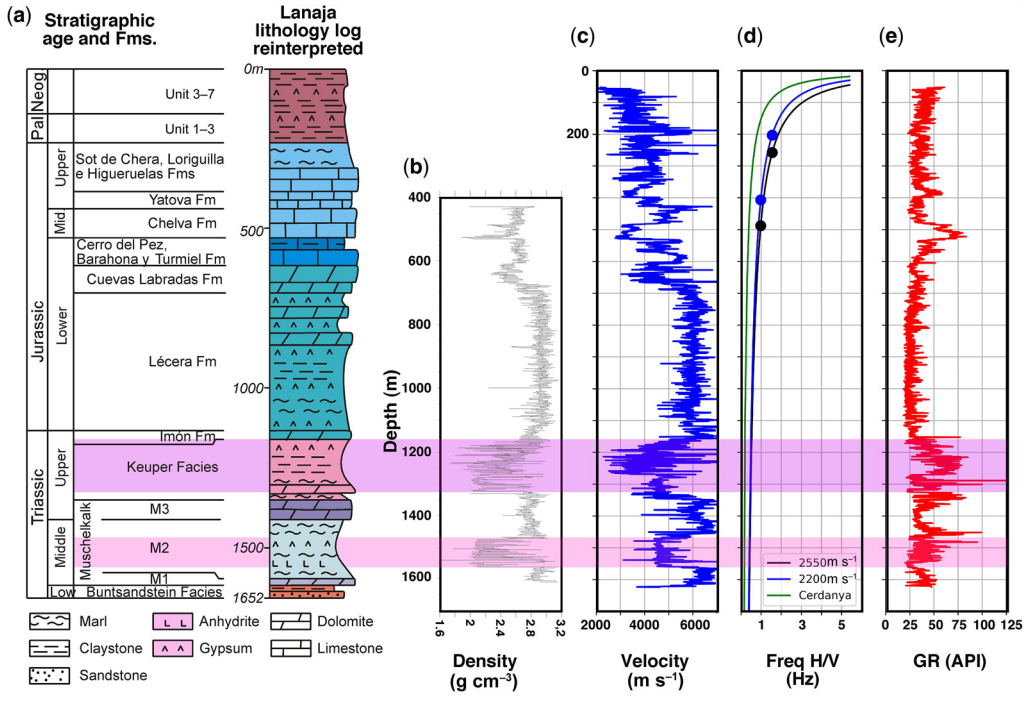

Fig. 4. (**a**) Stratigraphic column of Lopín-1 borehole. (**b**) Density log. (**c**) P-wave velocity (V_p). (**d**) Depth v. H/V frequency. Cerdanya relationship (green line) was based on geophysical measurements in the area (see Gabàs *et al.* 2016). Blue and black lines are two local relationships obtained for this study from Lopín V_p log and two average V_p values for the sector 0–53 m depth (blue line: 2200 m s^{-1}; black line: 2550 m s^{-1}). The V_s estimation model was Brocher (2005). Dots display depths obtained from each relationship and the frequencies of two peaks observed at the H/V curve at Lopín-1. H/V is the horizontal-to-vertical spectral ratio of ambient noise. (**e**) Gamma-ray (GR) log.

transparent package, while the Middle and Upper Jurassic are associated with a highly reflective package of continuous reflectors. The topmost unit is a medium to high reflectivity package with continuous and parallel reflectors that correlates with the Cenozoic deposits.

Passive seismic data–H/V method

The analysis of seismic noise is a valuable tool for subsurface characterization. Noise is related to ambient vibrations of the ground caused by different sources: tides, wind and anthropogenic noise sources such as cars, trains, industry, etc. (Bonnefoy-Claudet *et al.* 2006). Among other methods, the H/V method (horizontal-to-vertical spectral ratio of ambient noise method) has increasingly been used in several fields such as seismology, geotechnics or geology. This method is based on the recording of ambient noise in a three-component sensor, and computation of the ratio between the Fourier amplitude spectra of the horizontal and vertical components of seismic noise. The resulting spectral ratio is called an H/V curve whose amplitude peaks can be related to the presence of seismic impedance contrasts. The physical basis of this method has been controversial (Bonnefoy-Claudet *et al.* 2006). Some authors established a direct link between the shape of H/V curves and the S-wave resonance in the subsurface (Nakamura 2000), whereas other authors suggested that the shape of the H/V curves is controlled by the polarization of surface waves (e.g. Konno and Ohmachi 1998).

The standard way of obtaining H/V curves is to select stationary windows from a long record of ambient noise in a 3C sensor. Then, the Fourier amplitude spectra of the three components are computed and smoothed. The average of horizontal components is obtained and then, the horizontal-to-vertical spectral ratio is calculated for each window. Finally, the average H/V curve (and its standard deviation) is computed from the H/V curves calculated for all windows (Fig. 5).

Since the 1990s, several authors have introduced the H/V method as suitable for exploration studies (e.g. Ibs-von Seht and Wohlenberg 1999; Benjumea *et al.* 2011). These studies benefit from the relationship between the frequency corresponding to

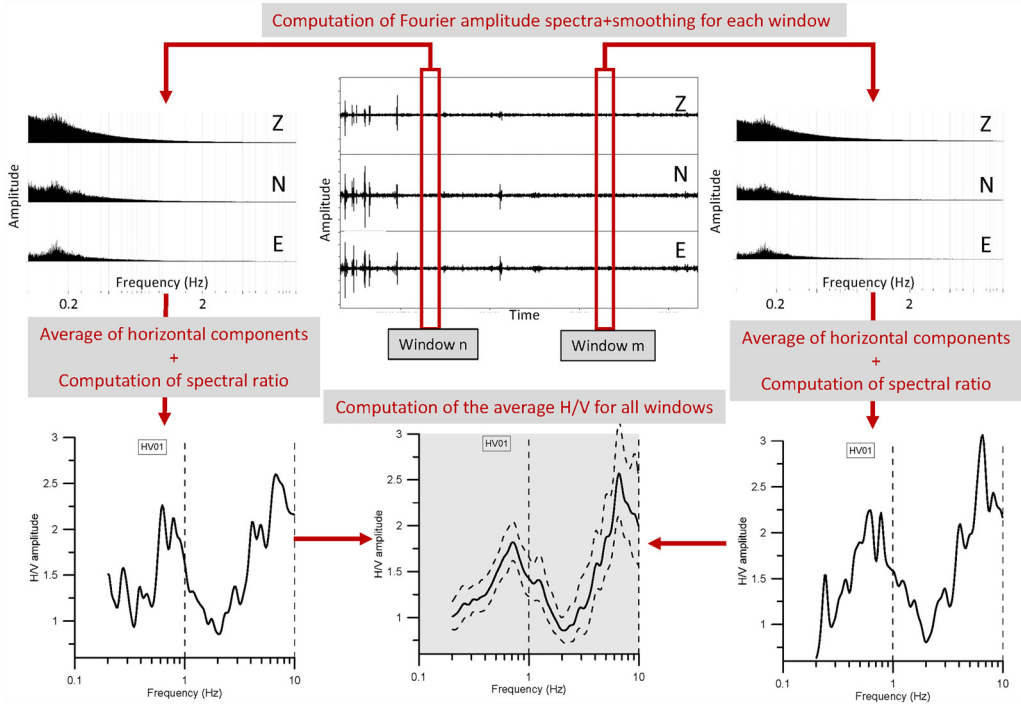

Fig. 5. Schematic of the procedure for obtaining H/V curves from ambient noise records. H/V is the horizontal-to-vertical spectral ratio of ambient noise.

amplitude peaks of the H/V curve ($f_{H/V}$) and the depth (h) of a contact with a significant impedance contrast (Gabàs *et al.* 2016). A relationship between these two quantities ($f_{H/V}$ and h) includes the average shear-wave velocity of the sediments (V_s):

$$f_{H/V} = \frac{\overline{V_s}}{4h} \quad (1)$$

Since shear-wave velocity information is not always available, another way of obtaining h is based on using an empirical relationship between h and $f_{H/V}$ (Ibs-von Seht and Wohlenberg 1999):

$$h = a f_{H/V}^{b} \quad (2)$$

where a and b are empirical parameters. This relationship is supported by the observations that the shear-wave velocity of unconsolidated overburden commonly exhibits a velocity gradient with depth. In this study area, we used the velocity gradient obtained from sonic logging at Lopín-1 borehole.

Ambient noise data were acquired along the studied reflection seismic profile at 12 locations spaced between 1 and 2.3 km (Fig. 1). Two additional stations were also located near Lopín-1 borehole for ground-truthing. The three stations at the SW end and at Lopín-1 borehole consisted of 120 s three-component Trillium Compact sensors and Spyder digitizers. Record length was 48 h and a sampling rate of 0.004 s. This long record was chosen in these locations to get datasets suitable for other ambient noise methods not included in this paper. The sensors, digitizers and batteries were buried in a pit. Data at the rest of the stations were acquired with a 5 s three-component sensor (Tellus, Lunitek) and Centaur Nanometric digitizer. For this dataset, record length was 2 h, suitable for the H/V method. Quality control was done in the field to check that the record length was enough to retrieve H/V curves.

The H/V curves were calculated using Geopsy software (http://www.geopsy.org; Wathelet *et al.* 2020). The complete record was cut in time windows with a length of 250 s. H/V curves were obtained for each window after Fourier transform of each component, smoothing and horizontal components averaging. The final H/V curves are the average of the horizontal-to-vertical spectral ratio of each window.

In order to transform the frequencies corresponding to H/V amplitude peaks into depth and constrain the interpretation of these main peaks, we obtained an empirical relationship (equation 2) using velocity information from the geophysical well logs from the Lopín-1 borehole. Beforehand, we had to correct erroneous values of slowness within the first 400 m due to an incorrect scale used during the digitization

process. We then calculated the compressional-wave velocity (V_p) log in m s^{-1}, obtaining 10 m interval velocity to downscale the geophysical logging to favour the comparison with H/V curves. Since the $f_{H/V}$–h empirical relationship is based on V_s, we obtained an interval V_s profile from interval V_p following different V_p to V_s relationships. In particular, we compared results from two V_s estimation models based only on V_p (Greenberg and Castagna 1992; Brocher 2005). The Brocher (2005) relationship was retrieved from V_p and V_s measurements compiled from borehole logs, vertical seismic profile (VSP), laboratory measurements and seismic refraction tomography studies from California. This relation is:

$$V_s = 0.7858 - 1.2344\ V_p + 0.7949 V_p^2 - 0.1238\ V_p^3 + 0.0064\ V_p^4 \quad (3)$$

On the other hand, Greenberg and Castagna (1992) proposed the following relationship to obtain V_p from V_s from coupling empirical relationships between shear- and compressional-wave velocities with Gassmann's equations:

$$V_s = -0.85588 + 0.80416\ V_p \quad (4)$$

For both equations (3) and (4), V_p and V_s are in km s^{-1}.

Since differences between these values fell within a range of 72 to 252 m s^{-1}, we decided to use Brocher (2005) as this is the most recent reference. The V_p to V_s transformation is one source of uncertainty that should be considered as coming from different factors such as the intrinsic limitation of the Brocher relationship obtained from a limited set of data information. Another issue when using well log velocity information is the lack of data from the shallow part of the well. The Lopín-1 borehole has velocity information from 53 m depth down to the bottom of the well. We assumed a V_p range for the shallow part (0–53 m depth) of 2200 to 2550 m s^{-1} based on velocity information for Tertiary sediments in the Ebro Basin. We calculated the average V_s-depth function using this V_p range for the shallower sector, and two different frequency–depth relationships using equation (2). For an average V_p of 2200 m s^{-1}, the resulting a and b parameters of equation (2) are 394.2 and 1.5, whereas for an average V_p of 2550 m s^{-}1, the values for a and b are 474.2 and 1.4. The plots for both $f_{H/V}$–h relationships are included in Figure 4. In this figure, another $f_{H/V}$–h relationship obtained for the Neogene basins in the NE of the Iberian Peninsula (Gabàs *et al.* 2016) was also included to highlight the importance of estimating local $f_{H/V}$–h relationships.

Gravity data: Bouguer anomaly and regional–residual separation

In the framework of the PilotSTRATEGY project and to enable linked interpretation of the available geophysical data, a regional gravimetric survey covering the study area with a distribution of two stations per square kilometre was carried out. Within this zone, some profiles with better data coverage (a station every 250 m) were also measured. Gravity data were acquired with an Autograv CG-5 (Scintrex) gravimeter. Tidal correction was automatically calculated by the instrument, based on Longman formulas (Longman 1959). Two bases tied to the International Standardization Network 1971 (IGSN71) were used. One of them (NGAB 635) (https://www.ign.es/web/ign/portal/gds-redes-nivelacion/-/redes-nivelacion/searchNetworkByName?searchByName=ends&textSearchByName=NGAB%20635) from the IGN's (National Geographical Institute, Spain) REDNAP (national high-precision levelling) network, and the other placed within the area specifically for this work and linked with the first base. The location of the stations, i.e. horizontal coordinates (x, y) and elevation (z), was measured with a differential GNSS (Global Navigation Satellite System) instrument (TRIUMPH from JAVAD) that has centimetric precision. Measurements were taken in three surveys from June to October 2021 with a total of 715 new stations. For quality control of the survey, 74 repetitions of coordinates and gravity were made that suppose around a 10.4% of the measurements with a mean square error of 0.036 m in x and y, 0.063 m in z and 0.02 mGal in gravity.

To obtain the Bouguer anomaly map, we followed the formulae from Hinze *et al.* (2005) (e.g. Ayala *et al.* 2016, 2021). For the calculation, we used the geodetic system GRS80 with orthometric heights with a density reduction of $\rho = 2.67$ g cm^{-3}. The terrain correction was applied up to 167 km distance. We used the CTT software developed by the geophysical division of IGME (Plata 2014), with some improvements from the ICGC (Cartographical and Geological Institute of Catalonia) based on Hammer sectors (Hammer 1939). Corrections from B, C and D sectors were obtained in the field. We used a 5 m DTM IGN regridded to 50 × 50 m for the sectors E to M; and a 200 × 200 m DTM IGN regridded to 400 × 400 m, completed with data from DSM EU-DEM (digital surface model–European Digital Elevation Model) of Copernicus for the French zone for the far distance terrain correction to 167 km, and bathymetric data from EMODnet (https://www.emodnet-bathymetry.eu/metadata-data).

In order to interpret the anomalies originated in the uppermost crust, the contribution from deeper sources has to be eliminated. A NE–SW regional gradient was assumed to correspond to lower crustal

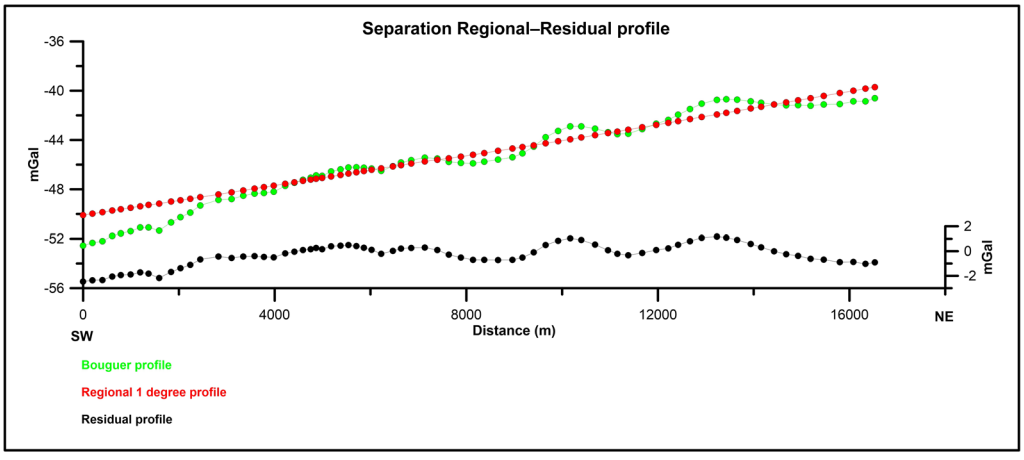

Fig. 6. Gravity data along ZA-7 and ZA-7-PROL (Bouguer anomaly in green, regional anomaly in red and residual anomaly in black). Please note that the scale for the residual anomaly is the one on the right.

structures, so a first-degree polynomial surface was fitted to the data points prior gridding as a regional anomaly. The residual anomaly was calculated by subtracting this regional field from the Bouguer anomaly. All the calculations were carried out directly on the data points prior to gridding.

The Bouguer anomaly, together with the regional and residual profile modelled for this work, corresponds to the observed profile (see Fig. 1 for location), as shown in Figure 6.

Petrophysical data

Petrophysical data are key information for modelling the potential field's geophysical data. Robust data on the target horizons are needed to limit the uncertainty of the geometrical model (Pueyo *et al.* 2021, pp. 103–152). To assign the densities for each of the model layers, we used data from the gamma–gamma (formation density) log from the Lopín-1 borehole (Fig. 4; Lanaja 1987) that was available for this study (from 425 to 1610 m depth, with more than 7700 readings), densities from 17 sites in the study area (mostly Cenozoic, Triassic and Permian rocks) that were measured in the Tres Cantos Laboratories and information from other Iberian Range studies (Pueyo *et al.* 2016; Izquierdo-Llavall *et al.* 2019 and references therein) containing more than 1500 sites with density estimates (Fig. 7).

Gravity modelling

We used the residual Bouguer anomaly as input data (data points along the studied profile; Fig. 1) since the geometrical structures the study aimed to constrain lie within the uppermost crust. The modelling was carried out using the GM-SYS module of the Oasis Montaj® software by Seequent. The algorithms of this module are based on the works of Talwani *et al.* (1959) and Won and Bevis (1987).

As the length of ZA-7 and ZA-7-PROL is only 17.5 km, it was extended by 200 km at both ends to avoid edge effects.

The observed anomalies mainly show a succession of highs and lows with amplitudes around 3–4 mGal that can be associated with the presence of

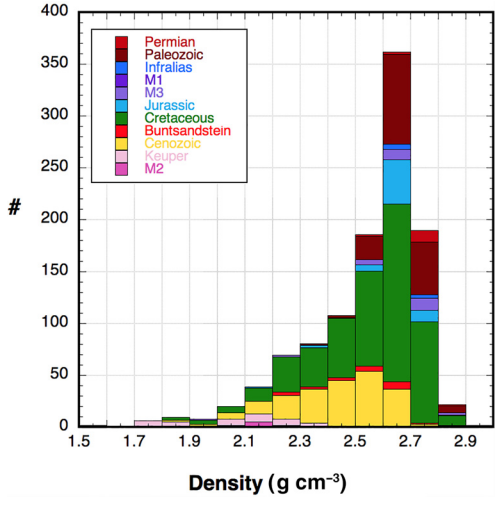

Fig. 7. Histogram of density data from outcrop hand samples of the Iberian Range database (including the data acquired in this project).

a series of horsts and graben below the M1. A gentle trend at the southern end of the profile could be attributed to an increase in thickness of the Tertiary cover.

Densities were obtained from the petrophysical data and considered constant for each lithology of the model. For the Purbeck facies, density was obtained from the same lithologies in the Hontomín 1, 2 and 3 boreholes (Ayala *et al.* 2011). The densities of the model are: Cenozoic: 2.45 g cm^{-3}; Cretaceous (Purbeck facies): 2.44 g cm^{-3}; Jurassic and Infra-Liassic (Imón Fm): 2.62 g cm^{-3}; anhydritic Jurassic: 3.0 g cm^{-3}; Keuper: 2.25 g cm^{-3}; M3 (dolomites): 2.80 g cm^{-3}; M2 (evaporites): 2.25 g cm^{-3}; M1 (anhydrite and dolomites): 2.90 g cm^{-3}; Buntsandstein: 2.58 g cm^{-3}; Paleozoic basement rocks: 2.68 g cm^{-3}.

The digitized cross-section obtained from the re-interpretation of the seismic profile was used as initial model, incorporating the results of the H/V interpretation as pseudo wells to add further constraints.

Results

Seismic reflection

In the studied reflection seismic line, the parallel reflectors that correspond to the M1 dolostones appear to have been disrupted by faults. Above that horizon, the seismic facies that correspond to the Middle Triassic evaporites (M2) shows strong lateral variations in thickness. In general, reflectors corresponding to the M3 dolostones, Upper Triassic evaporites (Keuper facies), dolostones of the Imón Fm and Jurassic strata show parallel reflectors with scarce disruptions and slightly folding. The Cenozoic rocks of the uppermost unit are represented by parallel reflectors, which are almost horizontal and show only slight lateral thickness variations.

The geometry interpreted from the seismic reflection profile is shown in Figure 3. The section has a basal succession of Paleozoic basement rocks, Buntsandstein facies and M1 dolostones affected by a series of normal faults forming several horsts and graben. Above this, the Middle Triassic evaporites (M2) show lateral thickness variations and act as a decoupling level above which the normal faulting is not observed. This is overlain by the M3 and Keuper facies together with the Jurassic–Cretaceous rocks, which show a series of gentle box folds accommodating the deformation that occurred below M2 (Fig. 3); the gentle anticlines coincide with the horsts and the synclines with the graben. At the top of the profile, Cenozoic strata overlap a roughly horizontal unconformity eroding the underlying Mesozoic rocks. Some small reverse faults have been interpreted; these are detached from the Keuper facies and affect the basal Jurassic rocks (Fig. 3).

Passive seismic results

Figure 8 shows the results obtained at two stations located in the vicinity of the Lopín-1 borehole. The H/V curves along the profile are displayed in Figure 9. All the curves are characterized by peaks with low H/V amplitude values for frequencies below 5 Hz. At higher frequencies, high amplitude peaks are observed for stations HV34 at 7.5 Hz, HV35 at 9.4 Hz and HV39 with a maximum at 5.1 Hz. The three stations were located over Holocene sediments, and these maxima are probably related to the base of Quaternary. Maximum thickness of the Quaternary deposits is found at HV39 station, located on the Ebro River terraces. The high amplitude of these peaks is a result of low velocity sediments at surface. Regarding the low amplitude peaks at frequencies lower than 5 Hz, the H/V curves obtained close to the well (Fig. 8) were used to select peaks in the rest of the profile. Two peaks that are consistent in both curves were interpreted using well information. As explained in the 'Data and methods' section, two different average V_p velocities (2200 and 2550 m s^{-1}) were used for the shallow part of the well to obtain the frequency–depth relationship from Lopín-1 borehole and the Brocher (2005) V_s estimation model. For simplicity, we will refer to these two relationships as 2200 $f_{H/V}$–h (blue line in Fig. 4) and 2550 $f_{H/V}$–h (black line in Fig. 4). The lower frequency maxima for both stations (Fig. 8) lie at 0.98 Hz. Using the two obtained $f_{H/V}$–depth relationships, the corresponding depth would lie between 406 and 488 m. These depths can be considered as bounds for seismic impedance contrast interpreted as a lithological change. The Lopín velocity log (Fig. 4) shows a sharp increment around 420 m depth, described as the contact between Upper and Mid-Jurassic strata. Hence, the low frequency maxima could reasonably be interpreted as a significant velocity contrast within the Jurassic deposits. The other maximum identified in Figure 8 corresponds to a frequency of 1.55 Hz. This can be related to a depth of 203 or 258 m using 2200 $f_{H/V}$–h or 2550 $f_{H/V}$–h relationships, respectively. The contact that produces this maximum can be interpreted as the transition from Cenozoic to Mesozoic strata (Fig. 4). The interpretation of these two peaks at Lopín-1 borehole was used to identify geologically meaningful H/V peaks along the profile and calculate a depth range for these two seismic impedance contrasts. The separation of these two peaks varies along the profile and, in particular at stations HV36 and HV37, only one wide peak is observed with a maximum around 1.2 Hz. This can be related to an approximation in

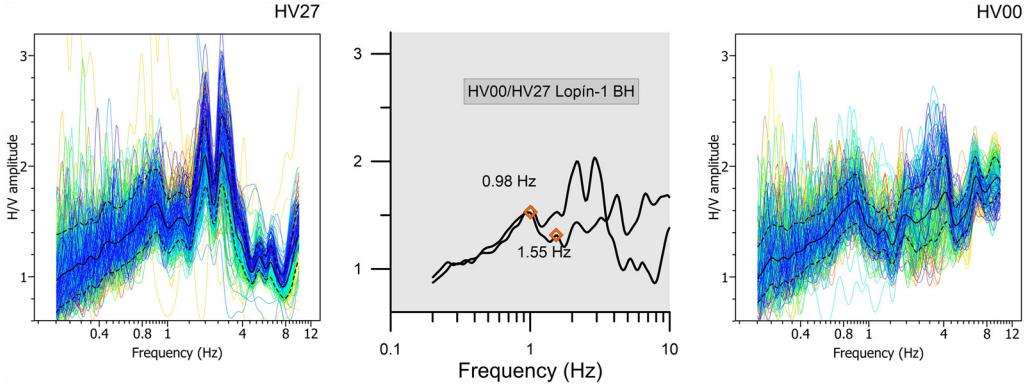

Fig. 8. H/V curves (colour lines) obtained for all the time windows at stations 27 and 00 located at the vicinity of the Lopín-1 borehole. Black and dashed lines represent the H/V average curve and standard deviation, respectively. H/V average curves for both stations (HV00 and HV27) are jointly plot in the centre figure to compare consistent maxima at the two stations. H/V is the horizontal-to-vertical spectral ratio of ambient noise.

depth of both contacts at this zone that cannot be resolved with the H/V method, as discussed in the 'Discussion and conclusions' section.

Gravity modelling

As described in the 'Data and methods' section, the cross-section was gravimetrically adjusted through a feedback process between seismic, geological and gravimetric modelling with the additional constraints of the petrophysical and H/V data (see workflow in Fig. 2).

The geometrical changes made to the initial model (Fig. 10a) in order to achieve the final model (Fig. 10b) mainly involved adjustments to the thickness of some units. The observed gravity anomaly was fitted by (1) assuming that the central and southern Cretaceous beds, whose existence is not clear from the seismic profile, are Purbeck facies, (2) deepening the central horst, (3) slightly varying the base of the Cenozoic in some parts of the profile, (4) varying the thickness of M2 which is justified by its evaporitic composition and (5) adding a layer of Jurassic strata with a high anhydrite content, increasing the density of this unit. This layer has been identified in the Lopín-1 borehole by an abrupt change in the V_p log and confirmed by the H/V method. This layer was modelled as a continuous unit with the same thickness throughout the cross-section.

In the case of the reservoir and seal units, the depths obtained from the seismic interpretation and the Lopín-1 borehole are consistent. This continuity is confirmed throughout the seismic profile even though the resolution is very poor. The thickness of the Triassic facies remains constant throughout the profile, as confirmed by interpretation of seismic and gravity data. The initial RMS of the difference between observed and calculated anomaly was 0.96 mGal, and the RMS for the final model is 0.15 mGal.

Discussion and conclusions

In the Lopín-1 structure, the targeted storage formation comprises detrital rocks of the Lower Triassic Buntsandstein facies. The seal comprises clays and evaporites of the Röt facies from the same period. These rocks, located below the M2 evaporitic level, are not well constrained by interpretation of the seismic reflection profile; they represent medium to high disrupted reflectors of low to medium quality; and the Paleozoic basement is represented by chaotic reflectors with scarce lateral continuity.

The innovative methodology applied here relies on geological modelling constrained by the integration of cost-effective techniques to improve storage formation characterization. To decrease the intrinsic uncertainties of gravity modelling, detailed petrophysical information from the Lopín-1 density log, new outcrop rock samples and regional databases were used to constrain density values of the subsurface. In addition, the H/V method provides information on the presence of significant seismic impedance contrasts in the top 500–600 m depth. This method requires geological and velocity data that in this study were provided by the Lopín-1 borehole. A detailed analysis of the relationship between H/V frequency, velocity and depth was included to obtain a local $f_{H/V}$–depth relationship suitable for this area. To our knowledge, this is the first time sonic logging has been used to estimate depths of impedance contrasts identified using H/V. The application of a local frequency–depth relationship is critical to obtaining reliable depths using the H/V method.

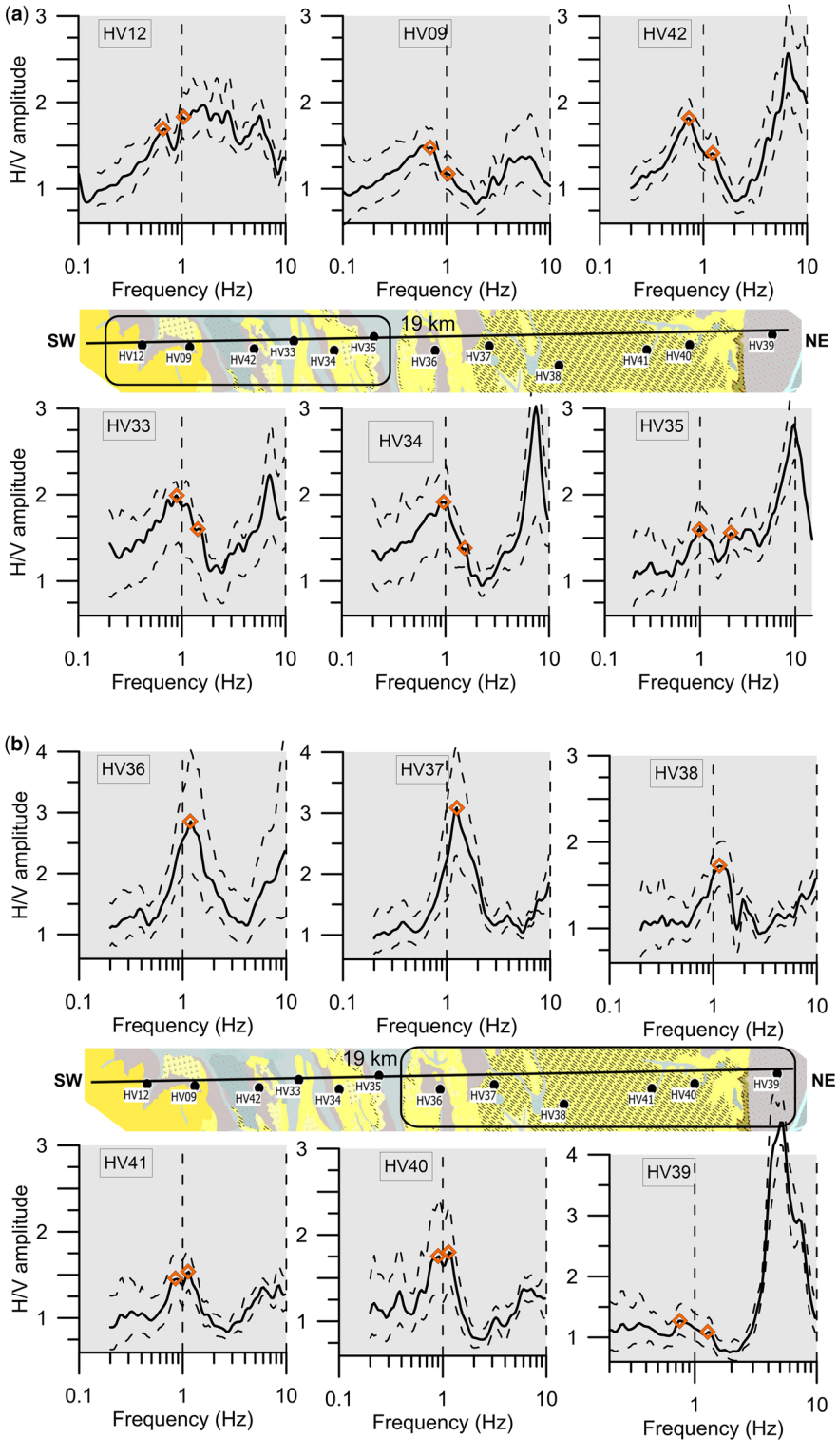

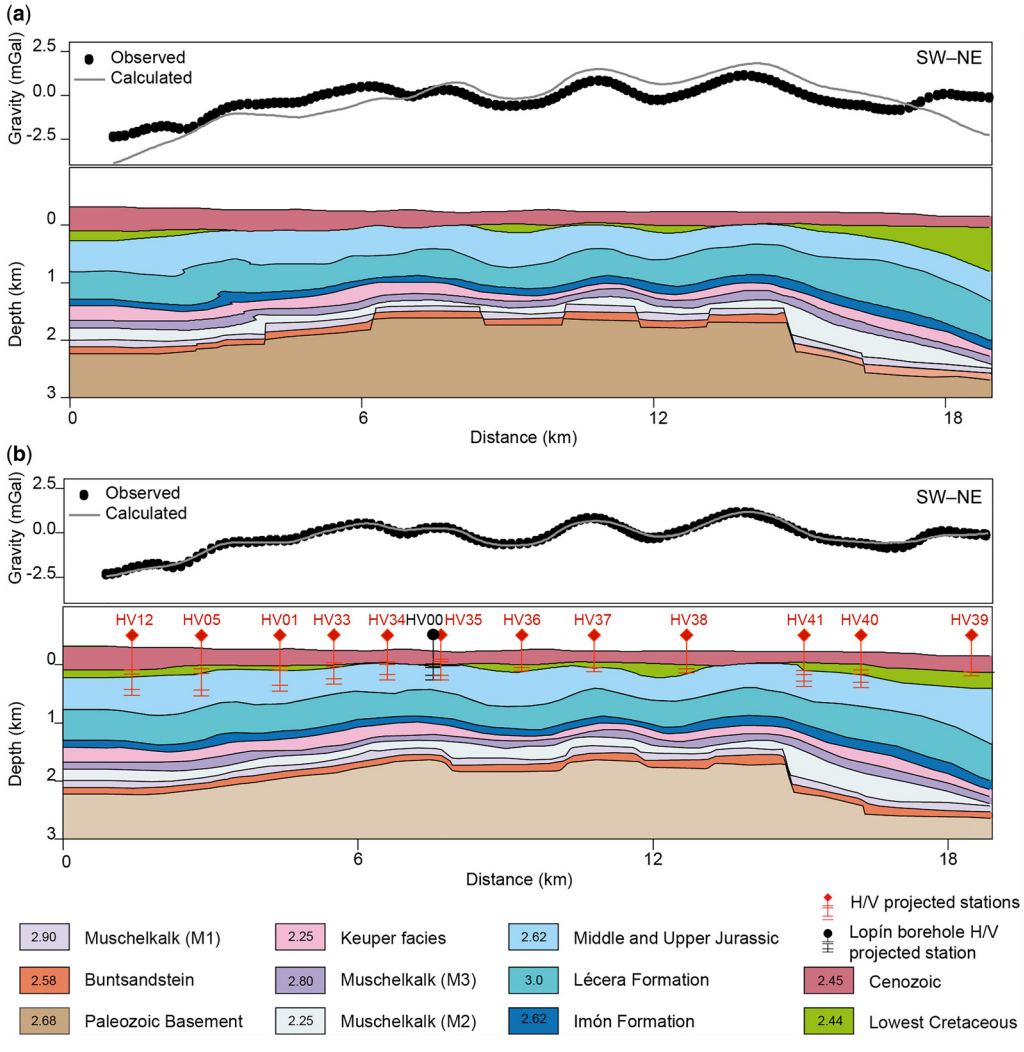

Fig. 10. (**a**) Initial geological cross-section based on the interpretation of the depth-converted seismic profiles ZA-7 and ZA-7-PROL. Please note that the corresponding observed and calculated gravity anomalies do not match. (**b**) Gravity-consistent geological cross-section taking into account H/V data and petrophysical data (density data used in the model are displayed in the unit boxes). Horizontal lines on the H/V data represent the maximum and minimum depths from the velocity range used. H/V is the horizontal-to-vertical spectral ratio of ambient noise.

However, depth uncertainty is also intrinsic to this method; in this study, uncertainty was generated by (1) estimation of shear-wave velocity from compressional-wave velocity and (2) lack of velocity information of the shallow part of Lopín-1 borehole, which is common in exploration boreholes. It should also be noted that, in this geological context, H/V peak amplitudes are low due to the relatively high velocity of Cenozoic sediments, and that plausible interpretation of the corresponding geological contacts requires appropriate geological borehole information. Two main peaks were analysed. Based on

Fig. 9. *Continued* H/V curves (continuous lines: average; dashed lines: standard deviation) corresponding to the six stations (**a**) at the SW sector of the profile and (**b**) at the NE sector. Legend of the geological map is shown in Figure 1. H/V amplitude scale was adjusted to improve clarity at each curve. Orange diamonds mark the peaks considered to be a result of geological features based on interpretation of the H/V curves acquired at the Lopín-1 borehole (Fig. 8). H/V is the horizontal-to-vertical spectral ratio of ambient noise.

data from the Lopín-1 borehole, the highest frequency peak was interpreted to be the base of the Cenozoic strata. The estimated depth for the lower frequency peak correlates with an intra-Jurassic velocity change in the Lopín-1 borehole. Nonetheless, at the northern end of the profile, this peak could also potentially be associated with the base of the Cretaceous strata.

The limits and uncertainty of the estimated depth for these two geophysical features (shown as two segments at each H/V location in Fig. 10b) were obtained from the two frequency–depth empirical relationships (2200 $f_{H/V}$–h and 2550 $f_{H/V}$–h). The depth range at each H/V station for the base of the Cenozoic along the profile and for the deeper seismic impedance contrast was used as constraint for gravity modelling, reducing uncertainties in the shallow section.

Figure 10b displays the location of the two seismic impedance contrasts on top of the geological cross-section. From this comparison, we observe the correspondence of the deepest contact, detected with the H/V method, to two different geological features. At the SW end of the profile, the deepest impedance contrast is coherent with an intra-Jurassic velocity change identified in the Lopín-1 borehole, as mentioned above. This change is associated with the transition between limestones and anhydrites, which results in a significant density change from 2.62 g cm^{-3} to 3.0 g cm^{-3}. However, this peak at the NE end of the profile seems to align with the base of the Cretaceous strata, an interpretation which is also consistent with the interpreted gravity data that reflect a change from a density of 2.45 g cm^{-3} of the Cretaceous to 2.62 g cm^{-3} of the Jurassic limestones. The shallowest feature coincides with the base of the Cenozoic layer, as also indicated by the gravity data, except at the HV36 site, where the H/V feature is located at the base of the small Cretaceous basin that is gravimetrically indistinguishable from the Cenozoic lithology since both packages have the same density.

The depth differences observed between the final gravity model and the H/V-estimated depths may be a result of shallow velocity variations along the profile. The lateral succession of higher and lower velocity shallow deposits (Holocene, Pleistocene, Neogene and Paleogene) influences the estimation of H/V depth, which was obtained with a single velocity relationship for the whole profile. To account for the uncertainties resulting from the use of this single calculated velocity, two different velocities were used to test the model fit with a range of parameters. Most of the modelled horizons lie within this range. Another issue that should be considered is the presence of high seismic impedance contrast that cannot be resolved by gravimetry. At the stations where two H/V peaks were identified, the difference in depth between the detected velocity contrast and the top of the anhydrite layer delineated by density contrast may be related to the presence of thin, high velocity layers within the Jurassic that are beyond the resolution of the gravity data.

The structural model interpreted from the seismic reflection profile is consistent with the observed gravity curve. The succession of symmetrical gravity highs and lows in the observed gravity anomalies fits well with a series of horsts and graben affecting the Paleozoic basement and Lower Triassic rocks (RMS of the difference between the observed and calculated is 0.16 mGal). The gravity response from hanging walls of thrusts is usually not as symmetrical as those shown in the studied profile, thus supporting the interpretation presented in this paper.

The results of this study highlight the efficiency of these cost-effective methodologies for subsurface characterization in CCS site investigations, particularly in areas with scarce and/or poor-quality seismic reflection data. The outcome of the modelling work resulted in an interpreted profile in which there is sufficient confidence; the authors believe that the application of this methodology on the entire structure will give a well-constrained image of the storage site, thus helping to decide on its suitability.

Acknowledgements The authors acknowledge the contribution of José María Llorente and Agustín González for their participation in the acquisition of the geophysical data. Thanks to Mario Ruiz and Jordi Díaz for their help in the preparation of the passive seismic surveys. We are grateful to Luis Cabañas from IGN for lending us some of the instrumentation used in the passive seismic surveys. We also thank the two anonymous reviewers for their thorough revision that helped to improve the manuscript.

Competing interest The authors declare that they have no known competing financial interests or personal relationships that could have appeared to influence the work reported in this paper.

Author contributions **CA**: conceptualization (lead), formal analysis (equal), investigation (equal), methodology (equal), validation (equal), visualization (equal), writing – original draft (equal), writing – review & editing (equal); **BB**: conceptualization (equal), formal analysis (equal), investigation (equal), methodology (equal), validation (equal), visualization (equal), writing – original draft (equal), writing – review & editing (equal); **JFM**: conceptualization (equal), formal analysis (equal), investigation (equal), methodology (equal), validation (equal), visualization (equal), writing – original draft (equal), writing – review & editing (equal); **JG-C**: conceptualization (equal), formal analysis (equal), investigation (equal), methodology (equal), validation (equal), visualization (equal), writing – original draft (equal), writing – review & editing (equal); **PC**: conceptualization (equal), formal

analysis (equal), investigation (equal), methodology (equal), validation (equal), visualization (equal), writing – original draft (equal), writing – review & editing (equal); **RS**: conceptualization (equal), formal analysis (equal), investigation (equal), methodology (equal), validation (equal), visualization (equal), writing – original draft (equal), writing – review & editing (equal); **FR**: conceptualization (equal), formal analysis (equal), investigation (equal), methodology (equal), validation (equal), visualization (equal), writing – original draft (equal), writing – review & editing (equal); **CR-M**: conceptualization (equal), formal analysis (equal), investigation (equal), methodology (equal), validation (equal), visualization (equal), writing – original draft (equal), writing – review & editing (equal); **ELP**: conceptualization (equal), formal analysis (equal), investigation (equal), methodology (equal), validation (equal), visualization (equal), writing – original draft (equal), writing – review & editing (equal); **JM-L**: data curation (lead), resources (equal), writing – review and editing (supporting); **AGG**: data curation (equal), resources (lead), writing – review & editing (supporting); **PF-C**: funding acquisition (lead), project administration (lead), supervision (lead), writing – original draft (equal), writing – review & editing (lead); **RM-O**: funding acquisition (equal), project administration (equal), supervision (equal), writing – review & editing (supporting).

Funding Funding for this research came from the Horizon 2020 Framework Programme (European Climate, Infrastructure and Environment Executive Agency (CINEA), award 101022664)

Data availability The datasets generated and analysed during the current study are available from the corresponding authors on reasonable request.

Appendix A: Software

Gravity data were processed to obtain Bouguer and residual anomalies using Oasis Montaj v. 9.7 from Seequent. The 2D gravity model was carried out using GM-SYS, an Oasis Montaj extension (https://www.seequent.com/es/productos-y-soluciones/geosoft-oasis-montaj/).

Time-to-depth conversion for the seismic section was processed using SKUA-GOCAD 19 (Emerson) (https://www.pdgm.com/products/skua-gocad).

GPS coordinates were calculated using Justin software (https://www.javad.com/jgnss/products/software/justin3.html).

Terrain correction was calculated using CTT software (Plata 2014). More information upon request to the corresponding author.

Regional map was calculated with REGRES software developed by IGME's geophysical area (Plata 2014). More information upon request to the corresponding author.

Passive seismic data analysis using H/V method was performed using Geopsy software (https://www.geopsy.org/).

References

Ábalos, B., Carreras, J. *et al*. 2002. Variscan and pre-Variscan tectonics. *In*: Gibbons, W. and Moreno, T. (eds) *The Geology of Spain*. Geological Society, London, 155–183, https://doi.org/10.1144/GOSPP.9

Alcalde, J., Flude, S. *et al*. 2018. Estimating geological CO_2 storage security to deliver on climate mitigation. *Nature Communications*, **9**, 1–13, https://doi.org/10.1038/s41467-018-04423-1

Alonso-Zarza, A.M., Armenteros, A. *et al*. 2002. Tertiary. *In*: Gibbons, W. and Moreno, T. (eds) *The Geology of Spain*. Geological Society, London, 293–334, https://doi.org/10.1144/GOSPP.13

Arenillas, A., Mediato, J.F. *et al*. 2014. *Atlas de Estructuras del Subsuelo Susceptibles de Almacenamiento Geológico de CO_2 en España*. Instituto Geológico y Minero de España.

Arlegui, L. and Simón, J.L. 2001. Geometry and distribution of regional joint sets in a non-homogeneous stress field: case study in the Ebro basin (Spain). *Journal of Structural Geology*, **23**, 297–313, https://doi.org/10.1016/S0191-8141(00)00097-3

Ayala, C., Rubio, F.M. and Rey-Moral, C. 2011. *Caracterización Microgravimétrica de la Estructura Geológica Seleccionada para Planta de Desarrollo Tecnológico de Almacenamiento Geológico de CO_2 en Hontomín (Burgos)* [Confidential]. Fondo documental del IGME, Código 64091.

Ayala, C., Bohoyo, F. *et al*. 2016. Updated Bouguer anomalies of the Iberian Peninsula: a new perspective to interpret the regional geology. *Journal of Maps*, **12**, 1089–1092, https://doi.org/10.1080/17445647.2015.1126538

Ayala, C., Rey-Moral, C. *et al*. 2021. Gravity data on the Central Pyrenees: a step forward to help a better understanding of the Pyrenean structures. *Journal of Maps*, **17**, 750–759, https://doi.org/10.1080/17445647.2021.2001386

Bachu, S. 2003. Screening and ranking of sedimentary basins for sequestration of CO_2 in geological media. *Environmental Geology*, **44**, 277–289, https://doi.org/10.1007/s00254-003-0762-9

Benjumea, B., Macau, A., Gabàs, A., Bellmunt, F., Figueras, S. and Cirés, J. 2011. Integrated geophysical profiles and H/V microtremor measurements for subsoil characterization. *Near Surface Geophysics*, **9**, 413–425, https://doi.org/10.3997/1873-0604.2011021

Benjumea, B., Gabàs, A., Macau, A., Figueras, S. and Bellmunt, F. 2016. Application of geophysical techniques to support geological mapping projects. *First Break*, **34**, 35–40, https://doi.org/10.3997/1365-2397.34.8.86172

Bonnefoy-Claudet, S., Cotton, F. and Bard, P.Y. 2006. The nature of noise wavefield and its applications for site effects studies: a literature review. *Earth-Science Reviews*, **79**, 205–227, https://doi.org/10.1016/j.earscirev.2006.07.004

Boot-Handford, M.E., Abanades, J.C. *et al*. 2014. Carbon capture and storage update. *Energy & Environmental Science*, **7**, 130–189, https://doi.org/10.1039/c3ee42350f

Brocher, T.M. 2005. Empirical relations between elastic wavespeeds and density in the Earth's crust. *Bulletin*

of the Seismological Society of America, **95**, 2081–2092, https://doi.org/10.1785/0120050077

Butillé, M., Ferrer, O. *et al*. 2012. Evidencias de deformaciones salinas en las sucesiones mesozoicas del sector sur de la Cuenca del Ebro. *Geotemas*, **13**, 176.

Gabàs, A., Macau, A., Benjumea, B., Queralt, P., Ledo, J., Figueras, S. and Marcuello, A. 2016. Joint audio-magnetotelluric and passive seismic imaging of the Cerdanya Basin. *Surveys in Geophysics*, **37**, 897–921, https://doi.org/10.1007/s10712-016-9372-4

García-Lobón, J.L., Reguera, M.I., Martín León, J., Rey Moral, C. and Berrezueta, E.R. 2010. *Plan de Selección y Caracterización de Áreas y Estructuras Favorables para el Almacenamiento Geológico de CO_2 en España: Resumen Ejecutivo*. IGME.

García-Quintana, A. 1977. Jurásico terminal y Cretácico inferior en la región central de la provincia de Valencia y noreste de la provincia de Albacete. *Seminario de Estratigrafía Serie Monográficas*, **1**, 1–334.

Gómez, J.J., Goy, A. and Barrón, E. 2007. Events around the Triassic–Jurassic boundary in northern and eastern Spain: a review. *Palaeogeography, Palaeoclimatology, Palaeoecology*, **244**, 89–110, https://doi.org/10.1016/j.palaeo.2006.06.025

Greenberg, M.L. and Castagna, J.P. 1992. Shear-wave velocity estimation in porous rocks: theoretical formulation, preliminary verification and applications. *Geophysical Prospecting*, **40**, 195–209, https://doi.org/10.1111/j.1365-2478.1992.tb00371.x

Hammer, S. 1939. Terrain corrections for gravimeter stations. *Geophysics*, **4**, 184–194, https://doi.org/10.1190/1.1440495

Hinze, W.J., Aiken, C. *et al*. 2005. New standards for reducing gravity data: the North American gravity database. *Geophysics*, **70**, J25–J32, https://doi.org/10.1190/1.1988183

Ibs-von Seht, M. and Wohlenberg, J. 1999. Microtremor measurements used to map thickness of soft sediments. *Bulletin of the Seismological Society of America*, **89**, 250–259, https://doi.org/10.1785/BSSA0890010250

Izquierdo-Llavall, E., Ayala, C. *et al*. 2014. *Informe de la Investigación del Reservorio Potencial de CO_2 'Zona de Enlace' (Cordilleras Ibérica y Costero Catalanas)*. IGME–IRMC.

Izquierdo-Llavall, E., Ayala, C. *et al*. 2019. Basement–cover relationships and their along-strike changes in the Linking Zone (Iberian Range, Spain): a combined structural and gravimetric study. *Tectonics*, **38**, 2934–2960, https://doi.org/10.1029/2018TC005422

Jurado, M.J. 1990. El Triásico y Liásico basal evaporíticos del subsuelo de la cuenca del Ebro. *In*: Ortí, F. and Salvany, J.M. (eds) *Formaciones Evaporíticas de la Cuenca del Ebro y Cadenas Periféricas y de la Zona de Levante*. Enresa, 21–28.

Klimowitz, J. 1992. Estratigrafía y disposición estructural del Terciario inferior en el subsuelo del sector central de la cuenca del Ebro. *Acta Geologica Hispanica*, **27**, 117–125.

Konno, K. and Ohmachi, T. 1998. Ground-motion characteristics estimated from spectral ratio between horizontal and vertical components of microtremor. *Bulletin of the Seismological Society of America*, **88**, 228–241, https://doi.org/10.1785/BSSA0880010228

Lanaja, J.M. 1987. *Contribución de la Exploración Petrolífera al Conocimiento de la Geología de España*. Instituto Geológico y Minero de España.

Leung, D.Y., Caramanna, G. and Maroto-Valer, M.M. 2014. An overview of current status of carbon dioxide capture and storage technologies. *Renewable and Sustainable Energy Reviews*, **39**, 426–443, https://doi.org/10.1016/j.rser.2014.07.093

Longman, M. 1959. Formulas for computing the tidal accelerations due to the moon and the sun. *Journal of Geophysical Research*, **64**, 2351–2355, https://doi.org/10.1029/jz064i012p02351

Mediato, J.F., García-Crespo, J. *et al*. 2014. *Informe del Estudio de los Posibles Reservorios de CO_2 'Lopín y Caspe'*. IGME-IRMC.

Mediato, J.F., García-Crespo, J. *et al*. 2015. Geological modelling of the Lopín CO_2 storage site, Spain. *Proceedings of the 8th European Congress on Regional Geoscientific Cartography and Information Systems*, 15–17 June. Institut Cartogràfic I Geològic de Catalunya, Barcelona, 104–105.

Mediato, J.F., García-Crespo, J., Izquierdo, E., García-Lobón, J.L., Ayala, C., Pueyo, E.L. and Molinero, R. 2017. Three-dimensional reconstruction of the Caspe geological structure (Spain) for evaluation as a potential CO_2 storage site. *Energy Procedia*, **114**, 4486–4493, https://doi.org/10.1016/j.egypro.2017.03.1608

Metz, B., Davidson, O., de Coninck, H.C., Loos, M. and Meyer, L.A. (eds) 2005. *IPCC2005 Special Report on Carbon Dioxide Capture and Storage*. Prepared by Working Group III of the Intergovernmental Panel on Climate Change. Cambridge University Press, Cambridge.

Mitjanas, G., Ledo, J. *et al*. 2021. Integrated seismic ambient noise, magnetotellurics and gravity data for the 2D interpretation of the Vallès basin structure in the geothermal system of la Garriga-Samalús (NE Spain). *Geothermics*, **93**, article 102067, https://doi.org/10.1016/j.geothermics.2021.102067

Nakamura, Y. 2000. Clear identification of fundamental idea of Nakamura's technique and its applications. *Proceedings of the 12th World Conference on Earthquake Engineering*, 30 January to 4 February, Auckland, New Zealand. New Zealand Society for Earthquake Engineering.

Ortí, F., Pérez-López, A. and Salvany, J.A. 2017. Triassic evaporitic of Iberia: sedimentological and palaeogeographical implications for the western Neotethys evolution during the Middle Triassic–Earliest Jurassic. *Palaeogeography, Palaeoclimatology, Palaeoecology*, **471**, 157–180, https://doi.org/10.1016/j.palaeo.2017.01.025

Pardo, G., Arenas, C. *et al*. 2004. La cuenca del Ebro. *In*: Vera Torres, J.A. (ed.) *Geología de España*. Sociedad Geológica de España e Instituto Geológico y Minero de España, 533–543.

Plata, J.L. 2014. Manual del programa CCT BLOQUES, informe inédito del Área de Geofísica. IGME. (Manual of the CCT BLOQUES software, unpublished report Geophysics Area, IGME).

Pueyo, E.L., Klimowitz, J.P. *et al*. 2010. Selección y caracterización de áreas y estructuras favorables para el almacenamiento geológico de CO_2 en España. *Volumen II-1 Cadena Pirenaica y Cuenca del Ebro – Geología*

(Atlas DINA2). Instituto de Reestructuración de la Minería del Carbón y Desarrollo Alternativo de las Regiones Mineras.

Pueyo, E.L., Izquierdo-Lavall, E. *et al*. 2016. Petrophysical properties in the Iberian Range and surrounding areas (NE Spain): 1-density. *Journal of Maps*, **12**, 836–844, https://doi.org/10.1080/17445647.2015.1084545

Pueyo, E.L., Ayala, C. *et al*. 2021. *Deliverable 6.4. Optimized 3D Reconstruction Workflow Based on Gravimetric, Structural and Petrophysical Data.* GEOERA 3DGEO-EU, 3D Geomodeling for Europe, project No. GeoE.171.005. Report, https://geoera.eu/wp-content/uploads/2021/11/3DGEO-EU_D6.4_Optimized-3D-reconstruction-workflow.pdf

Rogelj, J., Shindell, D. *et al*. 2018. Mitigation pathways compatible with 1.5°C in the context of sustainable development. *In*: Masson-Delmotte, V., Zhai, P. *et al.* (eds) *Global Warming of 1.5°C*. Intergovernmental Panel on Climate Change Special Report. Cambridge University Press, 93–174.

Sgattoni, G. and Castellaro, S. 2021. Combining single-station microtremor and gravity surveys for deep stratigraphic mapping. *Geophysics*, **86**, G77–G88, https://doi.org/10.1190/geo2020-0757.1

Sopeña, A., López-Gómez, J., Arche, A., Pérez-Arlucea, M., Ramos, A., Virgili, C. and Hernando, S. 1988. Permian and Triassic rift basins of the Iberian Peninsula. *Developments in Geotectonics*, **22B**, 757–786.

Stannard, D., Meyers, J., Turner, E. and Scopel, A. 2019. Update on the geophysical expression of the Abra sedimentary replacement Pb-Ag-Cu-Au deposit, Western Australia. *ASEG Extended Abstracts*, 20**19**, 1–7, https://doi.org/10.1080/22020586.2019.12073204

Stannard, D., Meyers, J. and Scopel, A. 2021. The Abra sedimentary-hosted Pb-Ag-Cu-Au deposit, Western Australia: a geophysical case study. *The Leading Edge*, **40**, 129–138, https://doi.org/10.1190/tle40020129.1

Talwani, M., Worzel, J.L. and Landisman, M. 1959. Rapid gravity computations for two dimensional bodies with application to the Mendocino submarine fracture zone. *Journal of Geophysical Research*, **64**, 49–59, https://doi.org/10.1029/JZ064i001p00049

United Nations 2015. *Paris Agreement. United Nations Treaty Collection. Chapter XXVII (7d)*. United Nations, https://treaties.un.org/pages/ViewDetails.aspx?src=TREATY&mtdsg_no=XXVII-7-d&chapter=27&clang=_en [last accessed December 12 2015].

Wathelet, M., Chatelain, J.-L., Cornou, C., Di Giulio, G., Guillier, B., Ohrnberger, M. and Savvaidis, A. 2020. Geopsy: a user-friendly open-source tool set for ambient vibration processing. *Seismological Research Letters*, **91**, 1878–1889, https://doi.org/10.1785/0220190360

Won, I.J. and Bevis, M. 1987. Computing the gravitational magnetic anomalies due to a polygon: algorithm and FORTRAN subroutines. *Geophysics*, **52**, 232–238, https://doi.org/10.1190/1.1442298